

RSC Advances



This is an *Accepted Manuscript*, which has been through the Royal Society of Chemistry peer review process and has been accepted for publication.

Accepted Manuscripts are published online shortly after acceptance, before technical editing, formatting and proof reading. Using this free service, authors can make their results available to the community, in citable form, before we publish the edited article. This *Accepted Manuscript* will be replaced by the edited, formatted and paginated article as soon as this is available.

You can find more information about *Accepted Manuscripts* in the [Information for Authors](#).

Please note that technical editing may introduce minor changes to the text and/or graphics, which may alter content. The journal's standard [Terms & Conditions](#) and the [Ethical guidelines](#) still apply. In no event shall the Royal Society of Chemistry be held responsible for any errors or omissions in this *Accepted Manuscript* or any consequences arising from the use of any information it contains.



Journal

PAPER

Controlled convective self-assembly of silver nanoparticles in volatile organic solvent and its application in electronics

Chengpeng Jiang,^a Li Li^a and Philip Wing Tat Pong^a

Received 00th January 20xx,
Accepted 00th January 20xx

DOI: 10.1039/x0xx00000x

www.rsc.org/

Fabricating functional materials with uniform properties and desired geometries using inorganic nanoparticles could offer us the ability to manufacture nanomaterial-built circuits or devices in a low-cost manner. In this work, we demonstrate a fabrication route combining nanoparticle assembly and sintering to produce uniform coatings and predefined patterns with high conductivity. Homogeneous coatings of monodisperse silver nanoparticles (Ag NPs) were assembled from their dispersion onto flat and non-functionalized substrates by convective self-assembly. The use of dodecylamine-capped 4.5 nm Ag NPs dissolved in chloroform ensures a low sintering temperature and a high evaporation rate. The introduction of syringe pump in the assembly process expedites the assembly rate in a controlled way as well as improves the surface morphology of the coatings. Heat treatment under facile conditions (200 °C, 15 min, in air) triggers nanoparticle sintering, making the Ag NP coating conductive. By changing experimental parameters, conductive coatings with different thickness (200–600 nm) and different conductivity ($1\text{--}3 \times 10^4 \text{ S cm}^{-1}$) could be produced on Si substrates. Wire bonding and flexible substrate tests show that the conductive coating is suitable for conventional electronics and flexible electronics. Conductive patterns of Ag NPs were fabricated by preparing conductive coatings on polyimide substrate with laser-engraved patterns. Application of the conductive patterns in electronics was demonstrated by connecting them as flexible electrodes to a magnetic field sensor. This controlled CSA technique expands the competencies of nanoparticle assembly, in terms of the size of deposition materials, the range of dispersing solvents, and the scope of potential applications.

Introduction

Fabricating devices and sensors using inorganic nanoparticles (INPs) through bottom-up processes have attracted considerable interests.^{1–4} INPs can be obtained through well-developed low-cost protocols of synthetic chemistry,⁵ and their optical, electrical and magnetic properties can be finely tailored by controlling their sizes and compositions.^{6,7} The key to the fabrication and application of functional materials and devices based on INPs is to create highly ordered and defect-free structures with homogeneous properties and well-defined geometries.^{8,9}

Various fabrication techniques have been developed to produce different structures (strips, coatings, patterns) utilizing INPs.^{9–12} Scanning probe lithography such as dip-pen nanolithography was employed to create predefined patterns with nanoparticle ink,^{13,14} achieving nanoscale resolution, but it is limited by the inadequate control of ink transport and deposition process.^{15–17} Drop-on-demand printing (inkjet printing) was widely applied for patterning complicated features using INP-based ink.^{18,19} Its printing performance is closely related to the viscosity and surface tension of carrier ink, and it may suffer from satellite drop or nonuniform drop

issues.²⁰ Transfer printing techniques (roll-to-roll gravure printing, flexographic printing, screen printing) were developed to deposit INPs on flexible or non-planar substrates with high yield and accurate placement in a rapid and parallel fashion.^{21–24} For these techniques, constraints on viscosity, polarity and volatility of the liquid ink are main considerations, and their molds need to be redesigned or programmable if printing patterns are changed.¹⁰ Film deposition methods (spin coating,²⁵ drop casting,²⁶ Langmuir-Blodgett technique²⁷) were applied to create nanoparticle coatings on flat substrates over large areas. They usually show low degree of controllability over structural parameters, and sometimes require special treatment of the substrates. Convective self-assembly (CSA) is a low-cost and easily implemented technique of nanoparticle deposition,^{28,29} which shows distinctive advantages: firstly, well-organized arrangement of nanoparticles could be achieved, making the assembled structures highly homogeneous;^{11,28} secondly, a wide range of solvents (aqueous, organic) could be used for dispersing different nanoparticles without modifying solvent properties^{30–32}; thirdly, the driving force of assembly process could be tuned by external stimuli (temperature, pH),⁹ directing surfaces (confined spaces, interfaces),^{8,33} or applied fields (magnetic).³⁴ Velev's group developed a controlled CSA technique by constantly dragging nanoparticle droplets confined in a moving meniscus between two plates, and multilayered coatings of Ag nanoparticles (12 or 16 nm) with different surface coverage

^a Department of Electrical and Electronic Engineering, The University of Hong Kong, Hong Kong. Email: ppong@eee.hku.hk
Electronic Supplementary Information (ESI) available: [additional figures]. See DOI: 10.1039/x0xx00000x

were deposited from aqueous suspension.^{35,36} Ressler *et al.* presented a similar CSA technique using meniscus-mediated horizontal deposition setups, and Au nanoparticles (18 nm) synthesized in aqueous phase were assembled as conductive wires with fine geometries and spacings on flexible substrates by stick-slip mechanism.^{37,38} Miyahara *et al.* incorporated a liquid-level manipulation system into the vertical-deposition CSA technique, which resulted in hierarchically ordered clusters, strips and girds composed of metallic nanoparticles (60 nm Au NPs, 80 nm Ag NPs).^{39,40} Although monolayered or multilayered structures of nanoparticles could be produced in these reports and other variations of CSA method, decreasing the assembly time, controlling the coating thickness (up to hundreds of nm) and creating predefined patterns while maintaining the assembled structures continuous and defect-free in CSA method still remain challenging.^{41,42} Besides, deficient research focuses on the assembly of sub-10 nm INPs, which are useful for electronics applications due to size effect and quantum confinement. Also, only a few protocols of CSA were established for non-polar organic solvents, which are commonly used to disperse INPs synthesized in organic phase.⁴³ To address these issues, we present a controlled CSA technique using ultra-small INPs dispersed in highly volatile organic solvent. This technique can be applied for the fabrication of homogeneous coatings and patterns formed by monodisperse INPs. Specifically, the use of volatile organic solvent increases the evaporation rate, promotes the convective flow and provides good dissolving ability for surfactant-capped INPs; the manipulation of liquid level by a syringe pump directly controls the assembly rate; the use of ultra-small INPs enhances the diffusion and mobility of nanoparticles; control of coating thickness was achieved by changing experimental parameters; predefined patterns of INPs were produced using polymeric substrate engraved by laser cutting. As for the deposition material, silver nanoparticle (Ag NP) was used due to its excellent conductivity, chemical stability and facile synthesis,^{44–47} and the assembled structure of Ag NPs can transform into conductive material by heat treatment, enabling us to evaluate its electrical conductivity and explore its application in electronics.

In this work, controlled CSA is achieved by a syringe-pump-assisted CSA technique. Monodisperse Ag NPs with 4.5 nm size capped by weakly bonded dodecylamine were synthesized as the building blocks, providing low sintering temperature and high electrical conductivity. Conductive coatings of Ag NPs were fabricated by depositing Ag NPs from their chloroform dispersion onto flat substrates using this controlled CSA technique together with facile heat treatment. Conductive patterns of Ag NPs used as sensor electrodes were fabricated by producing conductive coating on polyimide film with laser-engraved patterns. Microscopic morphology of the Ag NP coatings after the assembly process, nanostructure changes of the Ag NP coatings during the sintering process, and the influence of experimental parameters on the thickness and conductivity of the coatings were all investigated.

Experimental

Materials

Phenyl ether, dodecylamine, ethanol, and n-hexane were obtained from Acros Organics. 1,2-tetradecandiol and oleic acid were purchased from Sigma-Aldrich. Silver acetate was purchased from Sino-pharm Chemical Co., Ltd. All chemicals were of analytical grade and used as received.

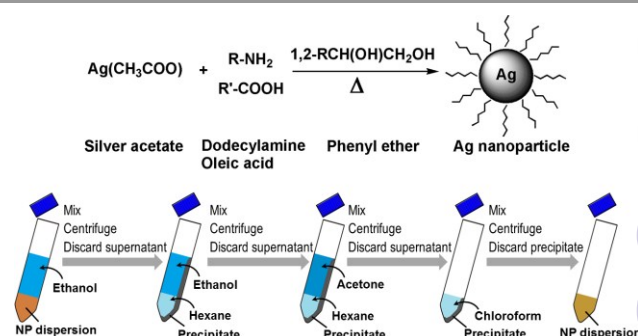
Synthesis and purification of Ag NPs

In a typical synthesis procedure of 4.5 nm Ag NPs, 3 mmol of silver acetate was added to a 50 mL beaker containing 60 mmol dodecylamine and 3 mmol oleic acid (Scheme 1). The mixture was gently heated to 40 °C and vigorously stirred using a magnetic stirrer for 15 min. During the dissolving of silver acetate, 40 mL phenyl ether and 6 mmol 1,2-tetradecandiol were added to a 100 mL flask and mechanically stirred under a gentle flow of nitrogen gas. This organic solution was heated to 140 °C at a heating rate of 10 °C min⁻¹ and maintained at this temperature. After the silver acetate was fully dissolved, the mixture of silver precursor and surfactants was rapidly injected into the flask containing the hot organic solution using a metal syringe. The reaction mixture was further heated to 200 °C at a heating rate of 10 °C min⁻¹, and kept at this temperature for 2 h. The resulting dispersion was cooled down to room temperature by removing the heat source.

Purification was performed for the obtained black-brown dispersion by mixing it with ethanol (2 volume equivalents) and centrifuged (3800 rpm, 10 min). The light brownish supernatant was decanted and the precipitated product was redispersed into 6 mL hexane. This washing process was repeated one more time. Acetone (2 volume equivalents) was then added to the dispersion, and a dark brown material was precipitated and separated by centrifugation. The precipitated product was dissolved in 6 mL chloroform, and centrifuged (3800 rpm, 10 min) to remove any undispersed residue.

Preparation of Ag NP coating by nanoparticle assembly

A syringe-pump-assisted CSA setup as illustrated in Fig. 1 was used for nanoparticle assembly to produce Ag NP coating. A pill box (bottom size: 18 mm × 20 mm) serving as the coating bath cell was fixed on a table, and a syringe pump equipped with a 1 mL syringe was placed nearby. A syringe needle was



Scheme 1 Schematic diagram for the synthesis and purification of Ag NPs.

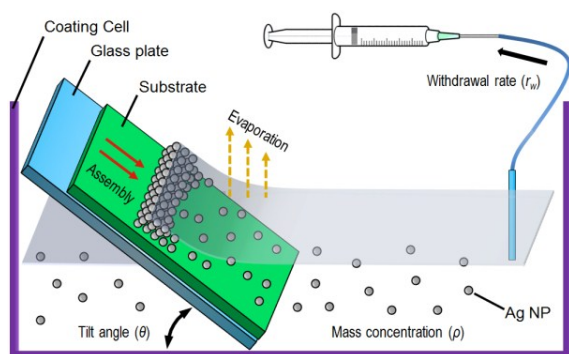


Fig. 1 Schematic illustration of the syringe-pump-assisted convective self-assembly (CSA) setup for nanoparticle assembly, with experimental parameters (r_w , ρ , θ).

vertically installed in the coating cell, and connected to the syringe via a flexible tube. A 4 mm × 6 mm Si substrate with native oxide layer was cleaned with acetone, ethanol and deionized water, and attached to a square glass slide cover, which serves as a supporting plate. They were then placed in the coating cell at a tilt angle θ of 22°. Subsequently, 800 μL chloroform dispersion of the Ag NPs with a mass concentration ρ of 37.5 mg mL^{-1} was slowly injected into the coating cell using a micropipette. The syringe pump was then turned on and operated at a withdrawal rate r_w of 50 $\mu\text{L min}^{-1}$. After all the dispersion was withdrawn, the coating cell was left drying for 10 min. Finally, a coating was obtained on substrate surface.

Formation of conductive coating by nanoparticle sintering

A heat treatment setup (Fig. S1) was used for nanoparticle sintering to produce conductive coatings. The sample with Ag NP coating was placed on a hot plate (Cimarec-HP131220, Thermo Scientific) covered with a flat sheet of aluminum foil. Two glass slides were placed to both sides of the sample to fix it. A curved piece of aluminum foil was overlaid on top of but without contacting the sample to reduce the heat dissipation. A glass petri dish was inverted and covered on the sample. By gradually increasing the temperature of the hot plate, the sample was heated to 200 °C at a rate of 10 °C min^{-1} , and then kept for 15 min. After this, the sample was cooled down to room temperature. Finally, a homogeneous coating with silver color was obtained on sample surface.

Fabrication of conductive patterns

Conductive patterns were fabricated on a polyimide substrate and connected as electrodes to a spintronic magnetic field sensor (GF-708, Sensitec, Germany). The fabrication process is illustrated in Fig. 2. At first, the CAD model of the electrodes was designed in SolidWorks. A polyimide film with thickness of 50 μm was then patterned (Fig. 2a) based on the CAD model using a laser cutting machine (VLS-2.30, Universal, USA). Parameters for this machine were adjusted to proper values (power: 6%, speed: 10%) so that the polyimide film was not fully cut through (Fig. 2g). Afterwards, conductive coating was produced on the patterned polyimide film through assembly and sintering of the Ag NPs (Fig. 2b). After this, the coated

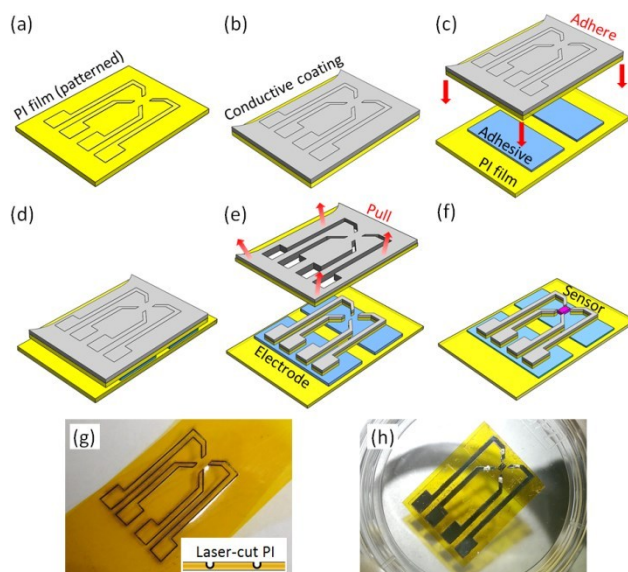


Fig. 2 Fabrication process of the conductive patterns: (a) patterning polyimide (PI) film by engraving the electrode outline using a laser cutting machine; (b) producing conductive coating on the patterned PI film; (c) adhering the coated PI film to a new PI film using adhesive tapes; (d) obtaining multi-layered films with conductive coating; (e) pulling off the top-layer PI film to detach electrode patterns; (f) interconnecting the sensor to the electrodes. (g) Optical image of the PI film with laser-engraved patterns, corresponding to (a); the inset illustrates its cross-section view. (h) Optical image of the sensor and the conductive patterns on PI substrate, corresponding to (f).

polyimide film was adhered to a new polyimide film using double-sided silicone adhesive tapes (Fig. 2c), producing multi-layered films with conductive coating (Fig. 2d). Then the top-layer polyimide film was slowly torn off, detaching the parts with electrode patterns (Fig. 2e). Four electrodes with maximum resistance of 5 Ω were obtained on the bottom-layer polyimide film. Following this, the magnetic field sensor was adhered onto the polyimide substrate, and its four contact pads were connected to the electrodes by wire bonding (Fig. 2f). The interface between the electrodes and the bonded wires were treated with commercially available conductive paint to enhance the attachment and reduce the contact resistance. Optical image of the sensor and the electrodes on polyimide substrate is shown in Fig. 2h.

Characterization

Morphological, structural and elemental characterization of the Ag NPs were performed by transmission electron microscopy (TEM), selected area electron diffraction (SAED) and energy dispersive X-ray spectroscopy (EDS) on an F-200 Tecnai-G2 TEM. Thermal properties of the Ag NPs were investigated using a TA Q50 thermal gravimetric analyzer (TGA) and a TA Q20 differential scanning calorimeter (DSC), both at a heating rate of 10 °C min^{-1} in nitrogen atmosphere. Ultraviolet-visible (UV-Vis) spectrum of the Ag NPs dispersed in chloroform was obtained with an Agilent Cary 60 UV-Vis. Surface morphology of the Ag NP coatings was analyzed using optical microscope (BX51, Olympus, Japan) and surface profilometer (Sloan, Veeco, USA). Surface structure and elemental composition of the conductive coatings were

investigated by scanning electron microscopy (SEM) and EDS with a Zeiss LEO-1530 SEM. Sheet resistance of the conductive coatings was measured using a custom-built 4-point probe platform (spring-loaded test probe, rectangular arrangement, spacing: 2.5 mm), and the corresponding conductivity was calculated using the geometric dimensions of the coatings.

Results and discussion

Synthesis of ultra-small and monodisperse Ag NPs

Inspired by the procedures published by Hiramatsu *et al.*⁴⁶ and by Peng *et al.*,⁴⁷ an improved synthesis protocol was developed to synthesize 4.5 nm monodisperse Ag NPs mainly capped by dodecylamine. In this reaction, Ag NPs were synthesized by thermolysis of silver acetate in organic phase, using dodecylamine and oleic acid as capping agents, and using diol as a reducing agent. Silver acetate was chosen as the precursor due to its good solubility in alkylamine. Dodecylamine was used as the main surfactant since it has a low boiling point (247 °C) and its amine group has weak interaction with the surface Ag atoms in Ag NPs.⁴⁷ This interaction can be broken up at relatively low temperature, enabling the coalescence of Ag NPs to form continuous and conductive structure.⁴⁸ Dodecylamine plays another role as a weak reducing agent at elevated temperature.⁴⁹ However, using dodecylamine as the sole surfactant in the reaction system led to polydisperse Ag NPs with large sizes (up to 10 nm) and low yield. To improve the quality of the Ag NPs, oleic acid was added as a co-surfactant because it facilitates the formation of monodisperse Ag NPs with ultra-small size (<5 nm), which is confirmed by our experimental results. The effect of oleic acid is probably related to the strong coordinate bond between the carboxylic group and the Ag atoms, and this bond may promote the formation of small-sized Ag nuclei as well as inhibit the further growth of existing Ag NPs.⁴⁷ Nevertheless, the high boiling point of oleic acid (360 °C) and the strong bond between oleic acid and Ag atoms make it difficult to remove oleic acid during the nanoparticle sintering process. Thus only a small amount of oleic acid was added in the reaction system. The rapid injection of the dissolved silver acetate and surfactants into the hot organic solution at 140 °C initiates the reduction of Ag precursor immediately. Heating the reaction mixture to a higher temperature (200 °C) for a long duration (2 h) facilitates the formation of Ag NPs.⁵⁰ Without adding diol, dodecylamine can provide a reductive environment for Ag precursor, but Ag NPs with bimodal size distribution were obtained. By introducing diol in the reaction, Ag NPs with uniform size were obtained without size-selection process, indicating that diol as a reducing agent influences the size distribution of Ag NPs. It is noteworthy that a dark color quickly appeared in the reaction mixture after the hot injection operation, and this dark color corresponds to the surface plasmon resonance (SPR) of the Ag NPs⁵⁰ formed in the mixture at a high concentration. This observation indicates that the formation of Ag NPs under these reaction conditions was a fast process.

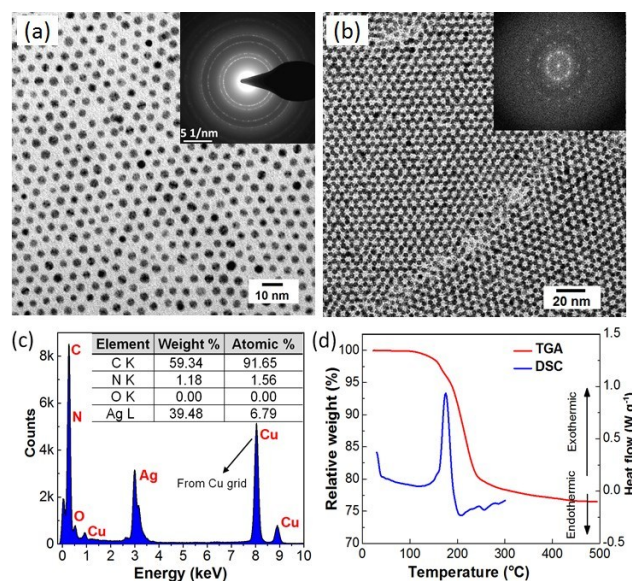


Fig. 3 (a) TEM image and SAED pattern (inset) of Ag NP array; (b) TEM image and FFT pattern (inset) of Ag NP superstructure; (c) EDS spectrum and elemental composition; (d) TGA and DSC of the Ag NPs.

Properties of the Ag NPs

Morphology, structure and composition of the Ag NPs were investigated by TEM. As shown in the TEM image in Fig. 3a, the 4.5 nm Ag NPs have a size distribution of 8%, close to 5% reported by Peng *et al.* for their synthesized 10.0 nm Ag NPs.⁴⁷ The inhomogeneous contrast reflected by the disordered arrangement of the dark spots in individual nanoparticles reveals the multifold-twinned structure of crystalline Ag.⁵⁰ SAED pattern for the Ag NPs is presented in the inset of Fig. 3a. The measured lattice spacing based on the diffraction rings match well with the *d*-spacing of corresponding (*hkl*) planes in bulk Ag (standard PDF database), indicating that the crystal structure of the Ag NPs is consistent with that of face-centered cubic (fcc) Ag. During sample preparation for TEM, two-dimensional superstructures were obtained by slowly drying Ag NP dispersion with high concentration on a copper grid covered by a petri dish, as presented in Fig. 3b. The highly ordered hexagonal stacking structures formed by two-layer nanoparticles and the symmetric bright spots in the fast Fourier transform (FFT) pattern of the superstructures (inset of Fig. 3b) are strong evidence that nanoparticles of uniform size were obtained and they have the tendency to self-organize into superstructures. The EDS spectrum in Fig. 3c shows the presence of Ag, O, N, C and Cu. Specifically, the Ag peak was generated by the Ag NPs; the O, N and C peaks were derived from the capping agents on the Ag NPs; the carbon-coated TEM copper grid contributed to the peaks of C and Cu. No other peaks related to any impurity were detected. Elemental compositions were derived by eliminating the Cu element, and the results show that the composition of the synthesized nanoparticles is Ag, and the capping agent is mainly dodecylamine with amine group. UV-Vis spectrum for colloidal

dispersion of Ag NPs shows an absorption peak at 415 nm (Fig. S2), in agreement with the literature report.⁴⁷

Thermal analysis was performed for the Ag NPs by TGA and DSC, and the results are presented in Fig. 3d. In TGA curve, a dominant weight loss was observed from 150 °C to 250 °C, and almost no weight loss was observed above 450 °C. TGA analysis shows that the Ag NPs contain more than 75 wt% silver. In the DSC curve, an intense exothermic peak at around 180 °C accompanied with continuous weight loss was observed. Desorption or evaporation of organic compounds typically shows endothermic behavior.^{51,52} This peak here may indicate that the exothermic effect of Ag NP sintering strongly outweighs the endothermic effect of dodecylamine desorption and evaporation. DSC analysis suggests that heat treatment at 200 °C is sufficient to trigger the sintering of the Ag NPs.

Convective assembly and morphology of Ag NP coatings

The assembly of colloidal particles through CSA technique is based on the convection of solvent due to evaporation, and this process drives the particles in the solvent to transport and deposit at the meniscus. Consequently, the particles assemble into ordered and closely packed coating. Directly implementing the CSA method by immersing a tilted Si substrate in our coating cell containing 800 μL dispersion of Ag NPs resulted in mosaic coating with cracks and voids, and the whole process was slow (~ 80 min). This may be attributed to that the evaporation rate of chloroform at the meniscus was quite fast while the contact line was actually translating at a low speed ($\sim 50 \mu\text{m min}^{-1}$). Thus excessive Ag NPs were continuously delivered there, making the nanoparticle concentration along the meniscus high and uneven. As a result, Ag NPs accumulated and deposited as nonuniform coating with crack patterns. The setups of CSA were improved by introducing a syringe pump to withdraw the dispersion, so the translation speed of the contact line can be increased and tuned ($150\text{--}400 \mu\text{m min}^{-1}$) by changing the withdrawal rate of the syringe pump ($25\text{--}100 \mu\text{L min}^{-1}$). Here the role of the syringe pump is to advance the convective assembly front, which is the three-phase contact line of the meniscus. By adjusting the withdrawal rate within a proper range, a steady state can be reached in which the translation of the assembly front is fast enough to balance the quick evaporation of chloroform at the meniscus. Under this condition, the local surface tension and nanoparticle concentration are uniform along the meniscus, and the Ag NPs self-assemble into a homogeneous coating. The total assembly time can be reduced to less than 20 min. Furthermore, some techniques were applied to optimize the syringe-pump-assisted CSA technique. Firstly, after the Ag NP dispersion was injected into the coating cell, the dispersion was allowed to evaporate for 30 s to initiate the assembly process. Secondly, the syringe pump was operated at a priming rate of $10 \mu\text{L min}^{-1}$, and then increased to a desired rate. Thirdly, a beaker was inverted and covered on the coating cell to reduce the evaporation rate of chloroform and prevent turbulent flow of air over the meniscus region.

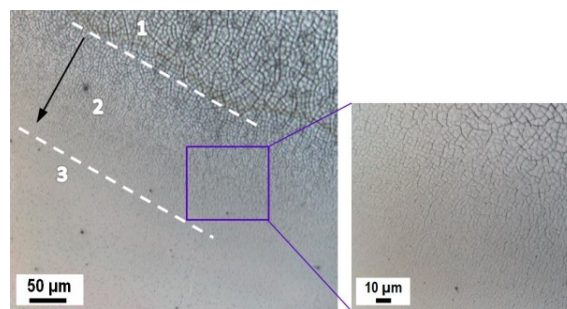


Fig. 4 Optical microscopy images of the Ag NP coating on Si substrate prepared with $r_w = 100 \mu\text{L min}^{-1}$, $\rho = 37.5 \text{ mg mL}^{-1}$, and $\vartheta = 22^\circ$. Images were taken near the edge of the coating. Regions 1, 2 and 3 reveal the morphological transition of the coating.

Optical microscopic observations of the Ag NP coating were performed to study its microscopic morphology. Fig. 4 is a representative image taken near the edge of the coating. Three distinct regions are delineated by the white dashed lines. Region 1 represents the initial coating obtained by direct CSA without using the syringe pump. Randomly oriented mosaic patterns sized from $5 \mu\text{m}$ to $10 \mu\text{m}$ were observed, and the coating surface is rough at micron scale. Region 2 represents the transitional coating obtained by starting the syringe pump and gradually increasing its withdrawal rate. The mosaic patterns shrink and evolve into smooth and homogeneous coating. The black arrow indicates the translation direction of the meniscus, and an enlarged image for the framed area in this region is also shown. Region 3 represents the final coating obtained by keeping the withdrawal rate of the syringe pump at $100 \mu\text{L min}^{-1}$. A continuous and compact coating with light grey color formed by self-assembled Ag NPs was obtained. The homogeneous appearance of this coating reflects its uniform thickness. Some dotted defects were also observed, probably caused by the impurities on the substrate surface and the resulting aggregation of the Ag NPs. Overall, the results demonstrate that the use of syringe pump promotes the formation of continuous and uniform coating.

To investigate how the experimental parameters affect the morphology of the Ag NP coating, three different groups of samples were prepared on Si substrates by the syringe-pump-assisted CSA technique, and characterized using optical microscope and surface profilometer. For the first group (Fig. 5a, b, c, d), different withdrawal rates of the syringe pump ($25, 50, 75, 100 \mu\text{L min}^{-1}$) were applied, while mass concentration of the Ag NP dispersion (37.5 mg mL^{-1}) and tilt angle of the substrate (22°) were unchanged. By increasing the withdrawal rate, the rough and coarse coating becomes flat and smooth, coupled with a decrease of the root-mean-square deviation of the roughness profile R_q . Withdrawal rate below $25 \mu\text{L min}^{-1}$ results in mosaic patterns similar to those in Region 1 of Fig. 4, while withdrawal rate above $150 \mu\text{L min}^{-1}$ leads to irregular island-shape patterns with large spacing due to the fast translation of the assembly front. For the second group (Fig. 5b, e, f), the substrates were tilted at different angles ($22^\circ, 32^\circ, 42^\circ$), while withdrawal rate ($50 \mu\text{L min}^{-1}$) and dispersion concentration (37.5 mg mL^{-1}) were unchanged. With the

increase of the tilt angle, the surface roughness and continuity of the coating becomes poorer, which may be caused by the insufficient attachment of the Ag NPs on substrate surface when the substrate is tilted too much. For the third group (Fig. 5g, h, i, b), Ag NP dispersions with different concentrations (18.75, 25, 31.25, 37.5 mg mL⁻¹) were used, while withdrawal rate (50 $\mu\text{L min}^{-1}$) and tilt angle (22°) were kept the same. The coatings prepared with dispersions of higher concentration are compact and continuous. However, mosaic patterns with size up to 10 μm appear in the coatings when dispersions of lower concentration were used. A minimum concentration of about 30 mg mL⁻¹ for the Ag NP dispersion is necessary to produce relatively smooth and homogeneous coatings. As a summary, higher dispersion concentration and smaller tilt angle lead to better coatings in terms of continuity and uniformity, and withdrawal rate affects the surface roughness of the coatings at the micron scale. All these three experimental parameters should be tuned within proper ranges to produce uniform coatings. Besides, the morphologies of the Ag NP coatings prepared here are quite different from the periodic strip patterns obtained by CSA method using nanoparticles

dissolved in aqueous or polar solvents.^{30,53–55} Such a difference derives from different solid-liquid interaction mechanisms⁵⁶ of these two methods (in our case, interaction between hydrophilic Si substrate and nonpolar chloroform), and the influence of solvent evaporation and nanoparticle diffusion should also be considered.

Sintering and nanostructure changes of Ag NP coatings

To study the nanostructure change and the resulting electrical conductivity of the Ag NP coating during the sintering process, three samples were prepared under the same assembly conditions but heated at different temperatures for 15 min. Nanostructure evolutions of the Ag NP coatings were investigated by SEM, as shown in Fig. 6a, b and c. Initially, at the first stage with a temperature of 160 °C, the Ag NPs are compactly packed on the substrate surface, and the homogeneous distribution of the Ag NPs reveals that the assembly process produced uniform coating at the nanoscale. Neck growth and grain growth were not observed at this stage, indicating that the organic capping agents on the Ag NPs were not fully desorbed, and this can also be inferred from the DSC analysis that 160 °C is lower than the onset temperature of the first exothermic peak. Subsequently, at the second stage with a temperature of 180 °C, large-sized Ag grains (60–80 nm) and small-sized Ag clusters (20–30 nm) appear, indicating that the capping agents on the surface of the Ag NPs began to desorb and evaporate. With the removal of the binding molecules, the Ag NPs contacted and connected together, developing into grains distinguished by boundaries. This nanoparticle coalescence process was driven by the minimization of free energy through surface area reduction.⁵⁷ Surface atom diffusion and internal recrystallization also contributed to this process.⁵⁸ Heat release associated with nanoparticle coalescence might enhance the coalescence rate,⁵⁷ as

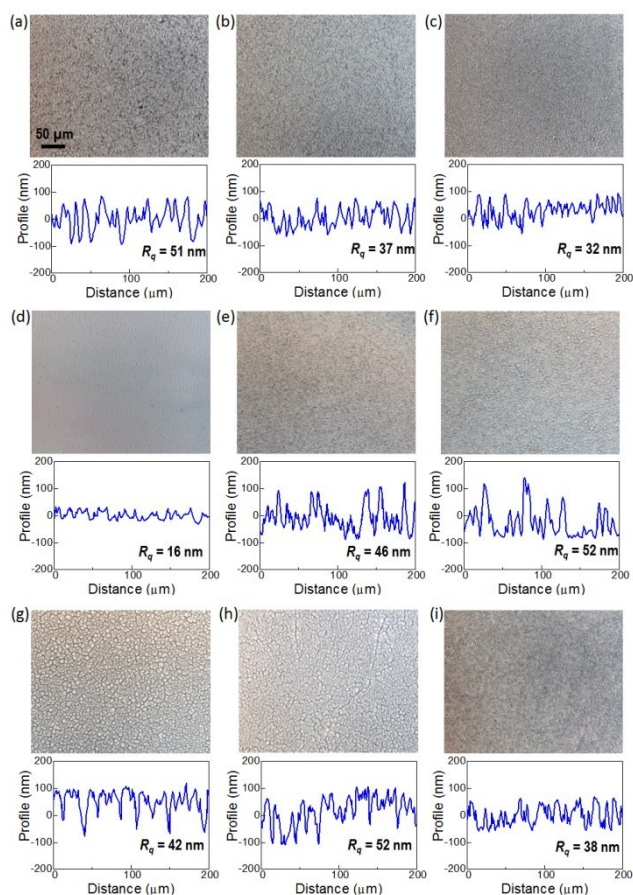


Fig. 5 Optical microscopy images and surface profiles of the Ag NP coatings on Si substrates prepared with (a) $r_w = 25 \mu\text{L min}^{-1}$, $\rho = 37.5 \text{ mg mL}^{-1}$, $\vartheta = 22^\circ$, (b) $r_w = 50 \mu\text{L min}^{-1}$, $\rho = 37.5 \text{ mg mL}^{-1}$, $\vartheta = 22^\circ$, (c) $r_w = 75 \mu\text{L min}^{-1}$, $\rho = 37.5 \text{ mg mL}^{-1}$, $\vartheta = 22^\circ$, (d) $r_w = 100 \mu\text{L min}^{-1}$, $\rho = 37.5 \text{ mg mL}^{-1}$, $\vartheta = 22^\circ$, (e) $r_w = 50 \mu\text{L min}^{-1}$, $\rho = 37.5 \text{ mg mL}^{-1}$, $\vartheta = 32^\circ$, (f) $r_w = 50 \mu\text{L min}^{-1}$, $\rho = 37.5 \text{ mg mL}^{-1}$, $\vartheta = 42^\circ$, (g) $r_w = 50 \mu\text{L min}^{-1}$, $\rho = 18.75 \text{ mg mL}^{-1}$, $\vartheta = 22^\circ$, (h) $r_w = 50 \mu\text{L min}^{-1}$, $\rho = 25 \text{ mg mL}^{-1}$, $\vartheta = 22^\circ$, and (i) $r_w = 50 \mu\text{L min}^{-1}$, $\rho = 31.25 \text{ mg mL}^{-1}$, $\vartheta = 22^\circ$. The scale bar in (a) is valid for all images. R_q is the root mean square of the surface profile.

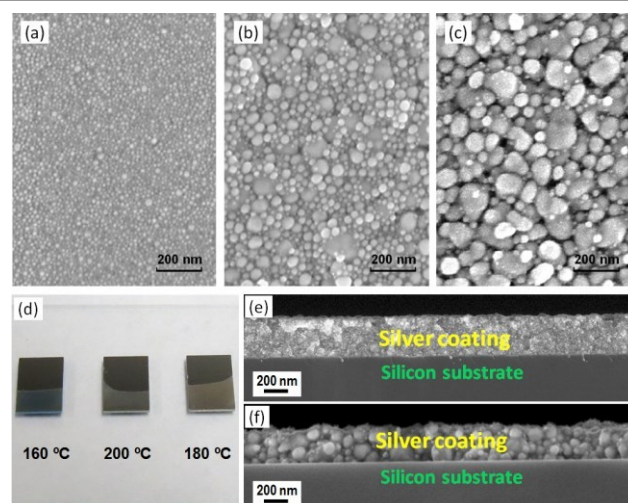


Fig. 6 SEM images of the Ag NP coatings on Si substrates prepared with $r_w = 50 \mu\text{L min}^{-1}$, $\rho = 37.5 \text{ mg mL}^{-1}$, $\vartheta = 22^\circ$, but treated with (a) 160 °C, (b) 180 °C, and (c) 200 °C, all for 15 min. (d) Optical images of the three coatings in (a), (b) and (c). Typical SEM cross-section images of an unsintered coating preliminarily treated at 160 °C (e) to remove organic substances and a sintered coating treated at 200 °C (f), both prepared with $r_w = 100 \mu\text{L min}^{-1}$, $\rho = 37.5 \text{ mg mL}^{-1}$, $\vartheta = 22^\circ$.

reflected by the sharp exothermic shape of the sintering peak in the DSC curve. There are still interspersed small-sized Ag NP clusters which did not participate in the coalescence process. The resulting coating at this stage is non-conductive because conductive paths were not completely formed. Finally, at the third stage with a temperature of 200 °C, considerable nanoparticle coalescence and grain growth were observed, resulting in the formation of large grains (up to 140 nm). These grains tend to share common interfaces and form continuous networks. The growth and fusion of Ag grains reduce the interface scattering and inter-particle tunneling of electrons,⁵⁹ leading to a significant enhancement of the conductivity.⁶⁰ The resulting coating at this stage is conductive ($\sigma = 3.15 \times 10^4 \text{ S cm}^{-1}$), indicating that conductive paths were completely formed in the coating. Additionally, elongating the sintering time to 30 min did not cause a remarkable increase in the conductivity of the coating ($\sigma = 3.70 \times 10^4 \text{ S cm}^{-1}$).

Optical image of the three coatings (Fig. 6d) shows their color difference. Typical SEM cross-section images of an unsintered coating preliminarily treated at 160 °C (Fig. 6e) to remove organic substances and a sintered coating treated at 200 °C (Fig. 6f) show that their surfaces are flat and their internal structures are continuous at nanoscale without cavity or pore. Lateral consistency of the coatings was evaluated by comparing their cross-section images taken at different locations (spaced at 1000 μm along the assembly direction) (Fig. S4). Both of the unsintered and sintered coatings demonstrate high degree of lateral consistency in terms of thickness, illustrating that the assembly technique could produce nanoparticle coatings with uniform thickness over millimeter-sized length, and this property of thickness consistency was well preserved after the sintering process. The fully sintered coating was further analyzed by EDS on SEM to identify its chemical composition. The results (Fig. S3) show that Ag and Si (comes from Si substrate) were detected, and no organic substances or silver compounds were detected. Hence, it can be inferred that after the sintering process, the organic materials were completely removed and the composition of the sintered coating is silver.

The sintering process (200 °C, 15 min) was applied for all the samples of Ag NP coatings prepared under different assembly conditions, and they all turned into silver color as a result. Characterization results obtained by optical microscope (Fig.

S5) show that the sintered coatings are uniform, and no obvious cracks or voids were observed.

Thickness and conductivity of conductive coatings

For the sintered Ag NP coating, its most important properties are thickness and conductivity because they both constitute the resistance and influence the electrical performance of the fabricated coating as conductive element. Here, the effect of experimental parameters on the thickness and conductivity of the sintered coatings were investigated.

As shown in Fig. 7a, raising the withdrawal rate of the syringe pump from 25 $\mu\text{L min}^{-1}$ to 100 $\mu\text{L min}^{-1}$ causes a roughly linear decrease of the coating thickness, together with an improvement of the coating quality, as reflected by the decrease of the error bar of the coating thickness. For the coating conductivity, it reaches a peak value when the withdrawal rate is 50 $\mu\text{L min}^{-1}$. This indicates that there may exist an optimal value or range of the withdrawal rate at which continuous coating with highest conductivity can be produced.

As shown in Fig. 7b, when the tilt angle of the substrate is increased from 22° to 32°, the coating thickness decreases slightly. As the tilt angle is further increased to 42°, its effect on the coating thickness becomes more significant. Tilt angles of 32° and 42° both lead to coatings with relatively low conductivity, probably due to the reduced continuity and increased roughness of the coating surface.

As shown in Fig. 7c, when the concentration of the Ag NP dispersion is decreased from 37.5 mg mL^{-1} to 25 mg mL^{-1} , the coating thickness shows a nearly linear decrease, coupled with a reduction of the coating conductivity. Further reducing the dispersion concentration leads to a relatively trivial decrease of the coating thickness, but causes a dramatic decline of the coating conductivity from $1.91 \times 10^4 \text{ S cm}^{-1}$ to $0.23 \times 10^4 \text{ S cm}^{-1}$. This indicates that the coating thickness may reach a minimum critical value ($\sim 120 \text{ nm}$), at which continuous coating with relatively high conductivity cannot form at macroscopic scale due to the low concentration of the Ag NP dispersion.

Overall, the coating thickness shows dependence on the three experimental parameters respectively, since they are all closely related to the assembly process. Another finding is that uniform coatings with high conductivity can be produced only when these parameters are altered within proper ranges. This can be explained by the fact that the self-assembly process has

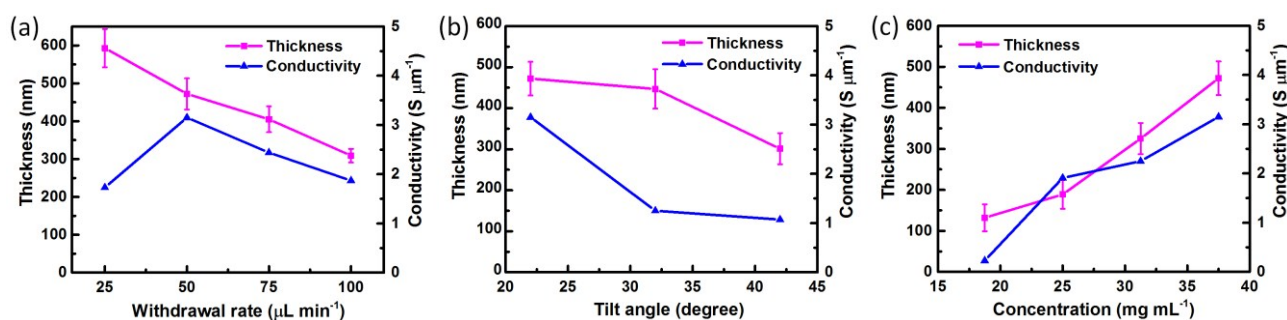


Fig. 7 Variation of the thickness and conductivity of the conductive coatings on Si substrates with (a) withdrawal rate of the syringe pump r_w , (b) tilt angle of the substrate ϑ , and (c) concentration of the Ag NP dispersion p . Assembly and sintering conditions for the conductive coatings are the same as those in experimental section if not specified. Error bars represent the standard deviation of the data.

nonlinear dynamics, and it is highly sensitive to initial conditions and experimental parameters,⁵⁶ and small variations can lead to coatings with different morphology and different conductivity. Moreover, the conductivity for most of the sintered coatings is in the range of $1\text{--}3 \times 10^4 \text{ S cm}^{-1}$, which is in the same order as that of a vapor-deposited Ag thin film ($4\text{--}6 \times 10^4 \text{ S cm}^{-1}$).⁴⁸ This level of conductivity is sufficient for applications in electronics, which typically requires conductivity of 10^2 S cm^{-1} to 10^5 S cm^{-1} .¹⁹ Additionally, by changing the experimental parameters appropriately, the coating thickness can be altered from 200 nm to 600 nm, while the coating conductivity is maintained at a high level ($>1 \times 10^4 \text{ S cm}^{-1}$). This is of great importance for designing and fabricating conductive elements with desired properties.

Wire bonding and flexible substrate test of conductive coatings

Wire bonding test was performed for the conductive coating fabricated on Si substrate. Before bonding test, a straight scratch was created all through the conductive coating using a sharp tip of titanium tweezers, so the coating was separated into two parts by a groove (inset of Fig. 8), and the resistance between the two separated coatings is very high ($>30 \text{ M}\Omega$) and they become essentially insulating. Then a manual wire bonder (HB05, TPT, Germany) was operated in the wedge bonding mode (bonding time: 103 ms, bonding force: 20 g), and

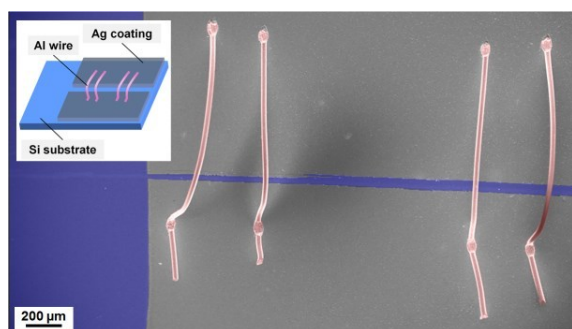


Fig. 8 SEM false-color image of Al wires bonded to the conductive coating on Si substrate. Assembly and sintering conditions for the conductive coating are the same as those in experimental section. Inset: a schematic illustration of the bonded wires.

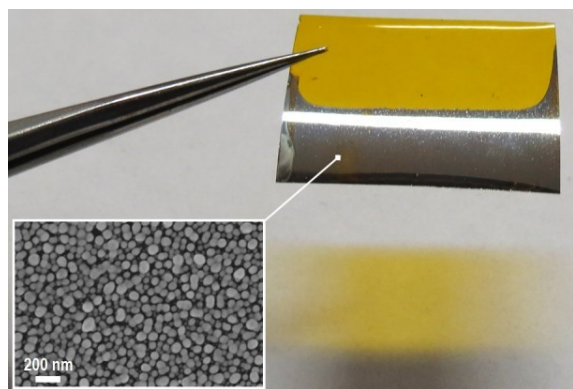


Fig. 9 Optical image of the conductive coating on PI substrate. Assembly and sintering conditions for the conductive coating are the same as those in experimental section, except volume of Ag NP dispersion: 1400 μL . The profile of the coating shows the shape of the meniscus. The inset is an SEM image of the conductive coating.

aluminum wires of 25 μm were pressed and adhered to the coating surface with ultrasonic energy applied. SEM image (inset of Fig. 8) shows that four wires (pink color, Al wire) were parallelly bonded to the conductive coatings across the groove (blue color, Si substrate). No separation or damage was observed at the interface between the conductive coating and Al wires. After wire bonding, the resistance between the two separated coatings is 1.36Ω , which is the total resistance of the Al wires, the conductive coating and the interfacial region. The success of wire bonding test shows that the conductive coating can withstand the ultrasonic force and pressure applied during wire bonding. Thus making electrical connections between the conductive coatings and electronic components can be achieved by wire bonding directly, and this is useful for integrating the nanoparticle-based conductive elements with conventional devices or sensors.

Flexible substrate test was performed by fabricating a conductive coating on polyimide substrate, as presented in Fig. 9. Ag NP coating was prepared by nanoparticle assembly on a Kapton HN polyimide film (thickness: 50 μm , size: 15 mm \times 18 mm). After heated at 200 $^{\circ}\text{C}$ for 15 min, a uniform coating with silver color was obtained on the flexible film. SEM image for this coating (inset of Fig. 9) shows that the Ag grains are quite uniform in terms of size and shape, unlike the grains formed in the coating prepared on Si substrate (Fig. 6c). This may be attributed to the different surface property and thermal property between polyimide substrate and Si substrate. The conductivity of the sintered coating on polyimide film is $1.2 \times 10^4 \text{ S cm}^{-1}$, and it remains almost unchanged after the polyimide film was bent ($\sim 20^{\circ}$). The feasibility of fabricating conductive coating using the Ag NPs on flexible film shows that this fabrication route can be applied in flexible electronics.

Performance test of the sensor connected to conductive patterns

The enlarged optical image of the conductive patterns

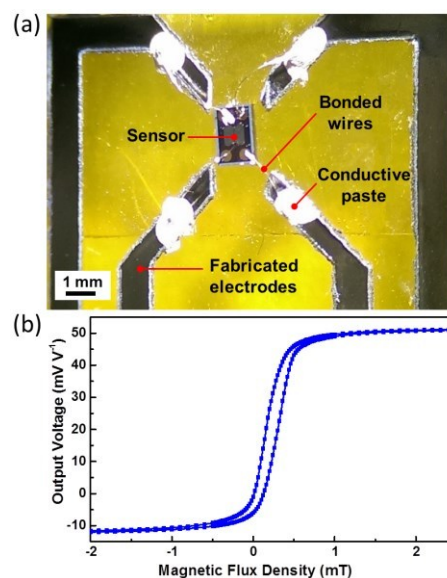


Fig. 10 (a) Enlarged optical image of the conductive patterns connected to the sensor on PI substrate. (b) Relation between output voltage of the sensor and applied magnetic flux density.

connected to the spintronic magnetic field sensor on polyimide substrate (Fig. 10a) shows that the minimum feature size of the conductive patterns is 0.7 μm . Performance test of the sensor was carried out by applying magnetic field generated from computer-controlled electromagnetic coils. Relation between the output voltage of the sensor and the applied magnetic flux density is presented in Fig. 10b. The transfer curve of this giant magnetoresistance (GMR) sensor exhibits characteristics of low hysteresis and high magnetic sensitivity. The measured sensitivity within the linear range is $128 \text{ mV V}^{-1} \text{ mT}^{-1}$, with a measured coercivity field (H_C) of 0.07 mT and a measured exchange coupling field (H_E) of 0.2 mT. These sensor performance results are similar to those specified in the datasheet of this sensor.

Conclusions

This work demonstrates a low-cost approach to fabricate conductive coatings and patterns formed by nanoparticles through controlled convective self-assembly and facile sintering of Ag NPs. The chemically synthesized Ag NPs are monodisperse, ultra-small and capped by dodecylamine, offering low sintering temperature and self-organizing property. In the nanoparticle assembly process, the use of chloroform as a volatile solvent ensures a high evaporation rate, and the introduction of syringe pump controls the assembly rate as well as improves surface morphology of the Ag NP coatings. The assembly process takes place in ambient environment and does not require functionalization of the substrate. The facile heat treatment (200 $^\circ\text{C}$, 15 min, in air) triggers sintering of the Ag NPs, leading to conductive structures. The coating fabricated on Si substrate is continuous and uniform, and its thickness (200–600 nm) and conductivity ($1\text{--}3 \times 10^4 \text{ S cm}^{-1}$) can be tuned by adjusting the experimental parameters within proper ranges. The conductive coating can be wire bonded directly and it is compatible with flexible polyimide substrate. The conductive patterns fabricated on laser-engraved polyimide film can be used as electrodes for sensors. The results of this work suggest that this controlled CSA technique stands out as a low-cost candidate for manufacturing nanomaterial-built elements and structures for both conventional and flexible electronics.

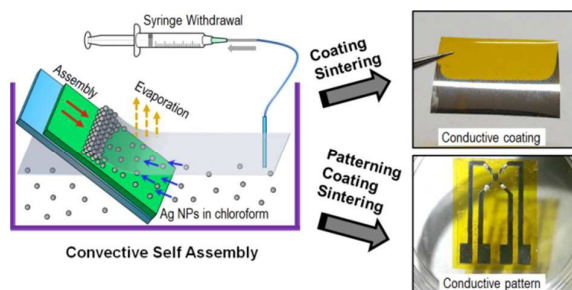
Acknowledgements

This work was supported in part by the Seed Funding Program for Basic Research and Small Project Funding Program from the University of Hong Kong, ITF Tier 3 funding (ITS/104/13, ITS/214/14), RGC-GRF grant (HKU 704911P), and University Grants Committee of Hong Kong (Contract No. AoE/P-04/08). Joeann Kwok is thanked for assistance in performing TGA and DSC experiment. Steven Zheng is thanked for conducting wire bonding test.

Notes and references

- 1 Y. A. D. Fernandez, T. A. Gschneidner, C. Wadell, L. H. Fornander, S. L. Avila, C. Langhammer, F. Westerlund and K. Moth-Poulsen, *Nanoscale*, 2014, **6**, 14605.
- 2 G. A. Ozin, K. Hou, B. V. Lotsch, L. Cademartiri, D. P. Puzzo, F. Scotognella, A. Ghadimi and J. Thomson, *Mater. Today*, 2009, **12**, 12.
- 3 A. Santos, M. Deen and L. Marsal, *Nanotechnology*, 2015, **26**, 042001.
- 4 Z. Nie, A. Petukhova and E. Kumacheva, *Nat. Nanotechnol.*, 2010, **5**, 15.
- 5 X. Wang, J. Zhuang, Q. Peng and Y. Li, *Nature*, 2005, **437**, 121.
- 6 T. K. Sau and A. L. Rogach, *Adv. Mater.*, 2010, **22**, 1781.
- 7 C. Rao, H. R. Matte, R. Voggu and A. Govindaraj, *Dalton T.*, 2012, **41**, 5089.
- 8 S. Kinge, M. Crego-Calama and D. N. Reinhoudt, *ChemPhysChem*, 2008, **9**, 20.
- 9 M. Curri, R. Comparelli, M. Striccoli and A. Agostiano, *Phys. Chem. Chem. Phys.*, 2010, **12**, 11197.
- 10 A. Carlson, A. M. Bowen, Y. Huang, R. G. Nuzzo and J. Rogers, *Adv. Mater.*, 2012, **24**, 5284.
- 11 A. Dong, J. Chen, P. M. Vora, J. M. Kikkawa and C. B. Murray, *Nature*, 2010, **466**, 474.
- 12 L. Li and Q. Wang, *ACS Nano*, 2013, **7**, 3053.
- 13 S.-C. Hung, O. A. Nafday, J. R. Haaheim, F. Ren, G. Chi and S. J. Pearton, *J. Phys. Chem. C*, 2010, **114**, 9672.
- 14 H.-T. Wang, O. A. Nafday, J. R. Haaheim, E. Tevaarwerk, N. A. Amro, R. G. Sanedrin, C.-Y. Chang, F. Ren and S. J. Pearton, *Appl. Phys. Lett.*, 2008, **93**, 143105.
- 15 B. Nelson, W. King, A. Laracuenta, P. Sheehan and L. Whitman, *Appl. Phys. Lett.*, 2006, **88**, 033104.
- 16 K. Salaita, Y. Wang and C. A. Mirkin, *Nat. Nanotechnol.*, 2007, **2**, 145.
- 17 K. A. Brown, D. J. Eichelsdoerfer, X. Liao, S. He and C. A. Mirkin, *Front. Phys.*, 2014, **9**, 385.
- 18 M. Singh, H. M. Haverinen, P. Dhagat and G. E. Jabbour, *Adv. Mater.*, 2010, **22**, 673.
- 19 W. Shen, X. Zhang, Q. Huang, Q. Xu and W. Song, *Nanoscale*, 2014, **6**, 1622.
- 20 S. Jeong, H. C. Song, W. W. Lee, Y. Choi and B.-H. Ryu, *J. Appl. Phys.*, 2010, **108**, 102805.
- 21 D. Sung, A. De La Fuente Vornbrock and V. Subramanian, *IEEE Trans. Compon. Packag. Technol.*, 2010, **33**, 105.
- 22 D. Deganello, J. Cherry, D. Gethin and T. Claypole, *Thin Solid Films*, 2010, **518**, 6113.
- 23 J. Noh, D. Yeom, C. Lim, H. Cha, J. Han, J. Kim, Y. Park, V. Subramanian and G. Cho, *IEEE Trans. Electron. Packag. Manuf.*, 2010, **33**, 275.
- 24 K.-S. Kim, Y. Kim and S.-B. Jung, *Nanoscale Res. Lett.*, 2012, **7**, 1.
- 25 K.-S. Chou, K.-C. Huang and H.-H. Lee, *Nanotechnology*, 2005, **16**, 779.
- 26 T. P. Bigioni, X.-M. Lin, T. T. Nguyen, E. I. Corwin, T. A. Witten and H. M. Jaeger, *Nat. Mater.*, 2006, **5**, 265.
- 27 V. Aleksandrovic, D. Greshnykh, I. Randjelovic, A. Fromsdorf, A. Kornowski, S. V. Roth, C. Klinke and H. Weller, *ACS Nano*, 2008, **2**, 1123.
- 28 Z. Cai, J. Teng, Y. Wan and X. Zhao, *J. Colloid Interf. Sci.*, 2012, **380**, 42.
- 29 L. Qian, S. Zhai, Y. Jiang and B. Das, *J. Mater. Chem.*, 2012, **22**, 4932.
- 30 C. Farcau, N. M. Sangeetha, N. Decorde, S. Astilean and I. Ressler, *Nanoscale*, 2012, **4**, 7870.
- 31 J. Ozhikandathil, S. Badilescu and M. Packirisamy, *J. Biomed. Opt.*, 2012, **17**, 0770011.
- 32 M. Pileni, *Phys. Chem. Chem. Phys.*, 2010, **12**, 11821.
- 33 T. Wen and S. A. Majetich, *ACS Nano*, 2011, **5**, 8868.

- 34 Y. Men, W. Wang, P. Xiao, J. Gu, A. Sun, Y. Huang, J. Zhang and T. Chen, *RSC Adv.*, 2015, **5**, 31519.
- 35 B. G. Prevo and O. D. Velev, *Langmuir*, 2004, **20**, 2099.
- 36 B. G. Prevo, J. C. Fuller and O. D. Velev, *Chem. Mater.*, 2005, **17**, 28.
- 37 C. Farcau, H. Moreira, B. Viallet, J. Grisolia, D. Ciuculescu-Pradines, C. Amiens and L. Ressler, *J. Phys. Chem. C*, 2011, **115**, 14494.
- 38 C. Farcau, H. Moreira, B. t. Viallet, J. Grisolia and L. Ressler, *ACS Nano*, 2010, **4**, 7275.
- 39 Y. Mino, S. Watanabe and M. T. Miyahara, *Langmuir*, 2011, **27**, 5290.
- 40 S. Watanabe, Y. Mino, Y. Ichikawa and M. T. Miyahara, *Langmuir*, 2012, **28**, 12982.
- 41 M. Grzelczak, J. Vermant, E. M. Furst and L. M. Liz-Marzán, *ACS Nano*, 2010, **4**, 3591.
- 42 Y. Masuda, T. Itoh and K. Koumoto, *Langmuir*, 2005, **21**, 4478.
- 43 R. Ye, Y.-H. Ye, Z. Zhou and H. Xu, *Langmuir*, 2013, **29**, 1796.
- 44 L. Li, J. Sun, X. Li, Y. Zhang, Z. Wang, C. Wang, J. Dai and Q. Wang, *Biomaterials*, 2012, **33**, 1714.
- 45 L. Li, F. Hu, D. Xu, S. Shen and Q. Wang, *Chem. Commun.*, 2012, **48**, 4728.
- 46 H. Hiramoto and F. E. Osterloh, *Chem. Mater.*, 2004, **16**, 2509.
- 47 S. Peng, J. M. McMahon, G. C. Schatz, S. K. Gray and Y. Sun, *Proc. Natl. Acad. Sci. USA*, 2010, **107**, 14530.
- 48 Y. Li, Y. Wu and B. S. Ong, *J. Am. Chem. Soc.*, 2005, **127**, 3266.
- 49 P. Li, Q. Peng and Y. Li, *Chem.-Eur. J.*, 2011, **17**, 941.
- 50 Y. Sun, *Chem. Soc. Rev.*, 2013, **42**, 2497.
- 51 H. Yu, L. Li and Y. Zhang, *Scripta Mater.*, 2012, **66**, 931.
- 52 K.-S. Moon, H. Dong, R. Maric, S. Pothukuchi, A. Hunt, Y. Li and C. Wong, *J. Electron. Mater.*, 2005, **34**, 168.
- 53 J. S. Jenkins, M. C. Flickinger and O. D. Velev, *Coatings*, 2013, **3**, 26.
- 54 C. Farcau, M. Potara, C. Leordean, S. Boca and S. Astilean, *Analyst*, 2013, **138**, 546.
- 55 Y. Masuda, T. Itoh, M. Itoh and K. Koumoto, *Langmuir*, 2004, **20**, 5588.
- 56 R. Toth, J. Heier, J.-N. Tisserant, E. E. Anna, A. Braun and T. Graule, *J. Colloid Interf. Sci.*, 2012, **378**, 201.
- 57 K. E. Lehtinen and M. R. Zachariah, *Phys. Rev. B*, 2001, **63**, 205402.
- 58 M. Jose-Yacamán, C. Gutierrez-Wing, M. Miki, D.-Q. Yang, K. Piyakis and E. Sacher, *J. Phys. Chem. B*, 2005, **109**, 9703.
- 59 A. Zabet-Khosousi and A.-A. Dhirani, *Chem. Rev.*, 2008, **108**, 4072.
- 60 Y.-L. Tai and Z.-G. Yang, *J. Mater. Chem.*, 2011, **21**, 5938.



A controlled convective self-assembly approach is reported for producing conductive coatings and patterns using ultra-small Ag nanoparticles in volatile solvent.